

**Direct-write Printing of a Self-Encapsulating Liquid Metal-Silicone Composite**

Journal:	<i>Soft Matter</i>
Manuscript ID	SM-ART-05-2020-000803.R1
Article Type:	Paper
Date Submitted by the Author:	12-Jun-2020
Complete List of Authors:	Neumann, Taylor; North Carolina State University Facchine, Emily; NC State University, Chemical and Biomolecular Engineering Leonardo, Brian; North Carolina State University, Chemical & Biomolecular Engineering Khan, Saad; North Carolina State University, Chemical and Biomolecular Engineering Dickey, Michael; North Carolina State University, Chemical & Biomolecular Engineering

## ARTICLE

## Direct-write Printing of a Self-Encapsulating Liquid Metal-Silicone Composite

Taylor V. Neumann,<sup>a</sup> Emily G. Facchine,<sup>a</sup> Brian Leonardo,<sup>a</sup> Saad Khan<sup>a</sup> and Michael D. Dickey<sup>a,\*</sup>

Received 00th January 20xx,  
Accepted 00th January 20xx

DOI: 10.1039/x0xx00000x

Silicone composites featuring inclusions of liquid metal particles are soft and stretchable materials with useful electric, dielectric, mechanical, and thermal properties. Until recently, these materials have primarily been cast as films. This work examines the possibility of using uncured liquid metal-elastomer (LME) composites as inks for direct writing. The liquid metal inclusions act as rheological modifiers for the silicone, forming a gel-structure that can be extruded from a nozzle and hold its shape after printing. Additionally, by tuning the particle size, larger particles in the printed structures can settle to form metal-rich regions at the bottom of the structures, encased by metal-depleted (insulating) regions. Using mechanical force, the liquid metal-rich interior can be rendered conductive by sintering without affecting the insulating exterior. Thus, it is possible to direct write print this soft and stretchable material while creating conductors with self-insulating shells.

### 1. Introduction

The enhanced properties that arise by combining two or more materials motivates the use of composites. For example, dispersing conductive particles (such as metals) throughout an elastomer can create a composite with increased thermal or electrical conductivity relative to pure elastomer.<sup>1,2</sup> Yet, the addition of such fillers typically stiffens the composite, thereby changing the mechanical properties. For emerging applications of soft robotics and stretchable electronics, this trade-off between mechanical and electrical / thermal properties is problematic. These applications benefit from materials that have enhanced electrical,<sup>3–5</sup> thermal,<sup>6</sup> and dielectric properties,<sup>7,8</sup> yet retain the soft and stretchable properties of the elastomer.

Liquid metals offer a possible solution to this trade-off because liquid metals are both metallic and soft (liquid like). Gallium and alloys of gallium have melting points at or near room temperature.<sup>9–11</sup> In this article we focus on a eutectic alloy of gallium and indium (EGaIn, 75.5 wt.% Ga, 24.5 wt.% In) which melts at 15.5°C. However, the physical behavior observed from EGaIn can be generally applied to other alloys of gallium sufficing they are in a liquid phase. This is due to the formation of a thin oxide surface layer (primarily composed of gallium oxide), which dominates the rheological behavior of these low melting point alloys.<sup>12</sup> Liquid metals exhibit both high conductivity and liquid-like stretchability.<sup>13</sup> This paper discusses a way to direct write soft and stretchable materials containing liquid metals, which is important for patterning them into useful shapes (wires, electrodes, antennas, thermal structures, actuators).

There are a variety of methods that can be used to pattern liquid metals including direct write printing<sup>14–17</sup>, however there are significant challenges with printing liquid metals directly. Extruding the metal from a nozzle produces spherical shapes due to the high surface tension of liquid metal. Although it is possible to stack such droplets to create shapes, the process is tedious. It is possible to directly print non-spherical shapes by shearing the metal from the nozzle, but this makes precise control of the distance between the nozzle and surface critical,<sup>18</sup> which can be challenging when working with substrates that are non-planar or have some surface roughness. One approach to make liquid metals easier to print is to mix in additional components to modify the flow behavior of the metal to make it easier to dispense it as a filament rather than as a spherical shape. This is usually realized by using a dispersion

<sup>a</sup>Department of Chemical and Biomolecular Engineering, North Carolina State University, Raleigh, NC, 27695 USA

\* Corresponding author.

Electronic Supplementary Information (ESI) available: [details of any supplementary information available should be included here]. See DOI: 10.1039/x0xx00000x

of solid particles (e.g. nickel,<sup>19</sup> tungsten,<sup>20</sup> or quartz particles<sup>21</sup>) in the bulk liquid metal phase. These additives change the rheological behavior to make the ink easier to print directly from a nozzle relative to pure liquid metal. These printed structures are still fluidic by nature and thus require some additional encapsulation steps to be useful for most applications. The encapsulation may be accomplished by casting silicone over the liquid metal,<sup>14,22,23</sup> printing an encapsulating polymer over the liquid metal<sup>24</sup>, or by co-printing a core-shell fiber which consists of a liquid metal core and insulating polymer shell.<sup>25–27</sup>

An alternative approach to forming structures containing liquid metal is to disperse liquid metal particles throughout an elastomer such as silicone.<sup>28–30</sup> Such composites form simply by mixing liquid metal into the uncured elastomer, as shown in **Figure 1a**. Upon curing the elastomer, a liquid metal elastomer (LME) forms with mechanical properties that are soft due to the low viscosity of the liquid filler. The modulus of the cured composite does increase slightly with the concentration of liquid metal inclusions; however, the increase is insignificant relative to the changes resulting from solid particle inclusions.<sup>31,32</sup> LMEs naturally exhibit a much higher thermal conductivity than the pure elastomer component, and this can be further improved by inclusion of additional material (e.g. graphene<sup>33,34</sup> or iron particles<sup>35</sup>) or by improving contact between the individual metal particles.<sup>31,36–38</sup> LMEs are not inherently electrically conductive due to the thin elastomer walls that separate the liquid metal droplets, which is useful for creating highly-loaded composites for dielectric applications<sup>31,39</sup> or thermal conductors that should not be electrically conductive. Yet, electrical conductivity can be induced by sintering the particles to form a percolated network. Sintering can be done by applying direct mechanical pressure to the LME (so-called “mechanical sintering”), causing the particles to rupture the thin silicone walls to form a connected electrical pathway.<sup>40–42</sup> Some recent efforts have used high loadings of liquid metal to make printable inks. They require an additional encapsulation layer to prevent liquid metal from leaking out from the composite under an applied force.<sup>43–46</sup> In this work, we aim to print patterns which are initially well-mixed but segregate into a liquid metal-rich zone in the interior and a liquid metal-depleted region on the exterior. This removes the need for additional encapsulation steps and prevents liquid metal from leaking from the composite.

These composites can be prepared by stirring manually or by using mixing equipment such as a high-shear mixer or blender. **Figure 1a** presents a schematic diagram of the initial unmixed materials. After mixing, the EGaIn breaks up into microparticles, dispersing throughout the silicone (polydimethylsiloxane, PDMS).

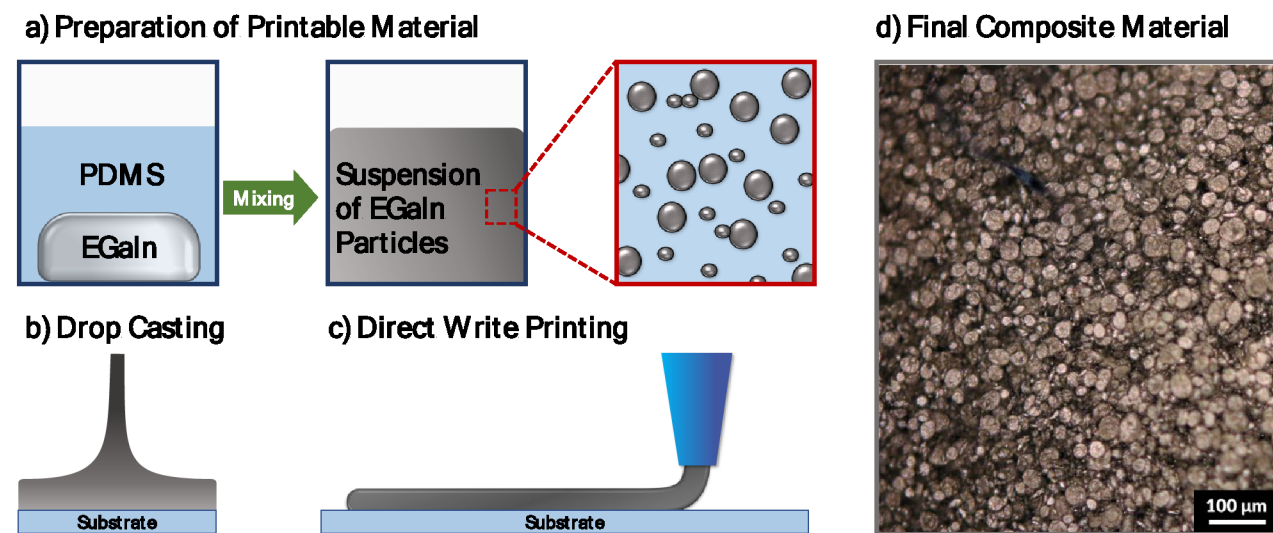


**Figure 1.** a) Schematic of preparation steps to create printable liquid metal elastomer (LME) composites from polydimethylsiloxane (PDMS) and liquid metal, eutectic gallium indium (EGaIn). b) When drop cast, the composite material spreads as a film at low particle concentrations. c) However, at sufficiently high particle concentrations, the material has gel properties and can be dispensed as a filament directly from a nozzle. d) Optical micrograph of the LME composite showing discrete liquid metal particles dispersed in PDMS. This sample was prepared at 90wt% EGaIn in PDMS and cast as a film.

In addition to enhancing the electrical and thermal conductivity of the composite, the liquid metal particles also function as rheological modifiers, which is important for direct write printing. Dispersing particles in PDMS increases the viscosity. Yet, at low particle concentrations, the viscosity of the dispersion remains sufficiently low that it flows when drop cast onto a surface, as seen in **Figure 1b**. Increasing the concentration of metal particles produces a gel-

like material well-suited for extrusion through a nozzle,<sup>43</sup> depicted schematically in **Figure 1c**. **Figure 1d** shows an optical micrograph of the cured LME, which contains discrete liquid metal particles. Here, we focus on tuning the rheology of such inks as a function of composition and demonstrate the ability to direct write LME. We also show that if the elastomer is left to cure slowly at room temperature, the metal in the printed structures can sediment to form structures that are insulating on the exterior and electrically conductive underneath.

## 2. Results and Discussion

### 2.1 Rheology

During direct write printing, the material experiences the largest shear stress as pressure forces it through the narrow constriction of the nozzle, but then experiences the lowest stress once it is outside of the nozzle. Thus, to make an ink compatible with direct write techniques, the material should flow from a nozzle in response to stress, but become self-supporting in the low-stress state after extrusion. For this reason, it is desirable to have inks that are shear-thinning (i.e., the viscosity decreases with shear) and have a yield stress (i.e., those that only flow above a critical stress). These properties can be realized in silicones by addition of another polymer or filler particles.<sup>47–51</sup> A similar effect is achievable by the addition of liquid metal.

We mixed liquid metal with PDMS (Sylgard-184, Dow) from 0 wt.% to 90 wt.% EGaIn (60 vol.% EGaIn) to determine the effect of composition on the rheology. Prior to conducting a systematic rheological investigation, we examined if the LMEs exhibited any thixotropic behavior when they are exposed to high shear. **Figure 2a** shows viscosity-shear rate profiles of representative samples in which the viscosity for each sample was measured across a range of shear rates. **Figure 2a** shows that the steady shear viscosity increases with increased loadings of EGaIn. This behavior is anticipated as we envision EGaIn to be a dispersion as observed from **Figure 1**, akin to that of colloids or emulsions.<sup>52,53</sup> We note here that the particles in this system are polydisperse, which may reduce the apparent viscosity compared to a monodisperse system.<sup>54</sup> Monodisperse liquid metal particle systems have been reported and could provide further control over the tuneable rheological properties.<sup>55</sup>

At lower EGaIn concentrations (e.g., 30 and 50 wt.%), the sample viscosity shows a Newtonian plateau; however these samples are not acting as hard spheres as the viscosity increase is higher than that predicted by the hard sphere model (**Figure S1, SI**).<sup>56</sup> The 70 wt.% EGaIn sample shows a substantial increase in its low shear viscosity indicating formation of internal structure. There is however the appearance of a Newtonian plateau in the viscosity suggesting that the structures are not interconnected. At the high EGaIn concentrations (e.g. 80 and 90 wt.%) we find the sample viscosities to increase even more. The lack of a Newtonian plateau signifies the formation of a sample-spanning network and possible presence of a yield stress. Thus, in addition to increasing the viscosity, the addition of liquid metal particles changes the viscosity profile from Newtonian (constant viscosity) to shear-thinning. This property is especially apparent for the samples with 70, 80, and 90% liquid metal. The presence of a shear-thinning viscosity and yield stress are both desirable properties for direct write printing.

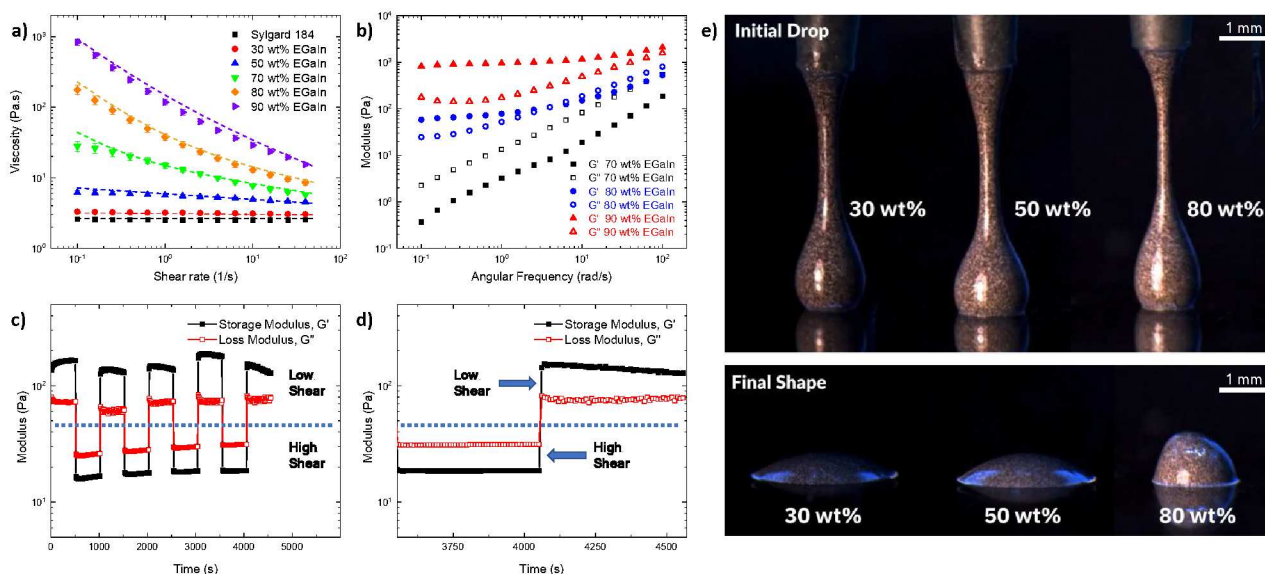


**Figure 2.** Rheological measurements of liquid metal particles suspended in silicone. a) Plot of the viscosity of the uncured liquid metal-silicone composites as a function of shear rate for varying concentrations of EGaln. The up-sweep is depicted by filled symbols and the down-sweep by open symbols. Dashed lines represent the model fit of a Herschel-Bulkley fluid. b) Plot of the moduli ( $G'$ ,  $G''$ ) of high concentration composites measured by frequency sweep at 0.02% strain. Gel-like behavior is observed above a concentration of 80 wt.% EGaln. c-d) Plot of the change in modulus for 90 wt.% LME at low strain and high strain (1% and 100%, respectively). At low strain the LME shows gel-like behavior, which ceases at high strain, allowing flow through a nozzle. After ceasing to apply the high strain, the material recovers the gel-like structure rapidly and can be cycled between states repeatedly without loss in mechanical properties. e) Images showing the difference in behavior of drops placed on a glass slide over time.

**Figure 2b** shows the frequency dependent behaviour of the elastic ( $G'$ ) and viscous ( $G''$ ) moduli of the three liquid metal samples with the highest concentrations of metal. We find the results to be consistent with the steady shear behaviour. For the 70 wt.% sample we find both  $G'$  and  $G''$  to be frequency dependent and almost parallel. This is reminiscent of samples close to but not yet at the gel point based on the Winter-Chambon criteria,<sup>57,58</sup> just as we observed in the steady shear mode. At 80 wt.% EGaln the LME begins to display behavior indicative of a 'weak' gel; the  $G'$  is larger than  $G''$  at low frequencies and both moduli plateau with decreasing frequencies. At 90 wt.% EGaln,  $G'$  is significantly larger than  $G''$  and both are relatively flat for a wide range of frequencies, indicating gel-like behavior.<sup>59</sup>

Given the elastic-like nature of the 80 and 90 wt.% sample, we expect these to exhibit yield stresses. We find the values of the yield stress for 80 and 90 wt.% samples to be 16 Pa and 64 Pa respectively (seen in **Figure S2, SI**) obtained via fitting a Herschel-Bulkley model, given in Equation 1 below, to the data.

$$\tau = \tau_0 + k\dot{\gamma}^n \quad [1]$$

Here  $\tau$  represents the shear stress,  $\tau_0$  is the yield stress, and  $k$  and  $n$  are the consistency and flow indices, respectively. The yield stress values are substantially lower than the estimated 0.1-1 GPa yield stress of the metal oxide of the particles,<sup>40</sup> indicating the required stress to incite flow in the LME is much lower than that required to break the oxide, further corroborating our notion that EGaln acts as colloidal dispersions.

Since our goal is to observe the utility of LMEs as a direct writable ink, it was encouraging to find that the LME displays gel-like behavior at low stress and flows at high stress. We sought to ensure that the initial internal structure could be regained after dispensing from a nozzle to prevent the ink from spreading. We placed a sample of 90 wt.% EGaln under alternating sets of high and low oscillatory strain (100% strain and 1% strain, respectively) at a constant angular frequency of 1  $\text{rad}\cdot\text{s}^{-1}$ . At low strain, the sample exhibits gel-like behavior, with  $G'$  greater than  $G''$ . At high strain (similar to that experienced when being extruded through a nozzle),  $G''$  was greater than  $G'$ , indicating breakdown of the sample microstructure.<sup>60</sup> Upon removing the high strain, the structure recovers with a higher modulus. Changing between these two states is repeatable, as seen in **Figure 2c**. There is a slight variation with time and between cycles for the recovered modulus values, but this not significant compared with the increase in modulus upon cessation of shear. **Figure 2d** shows a closer look at one of the transition points from high to low shear and shows the structure

recovers almost instantaneously even after multiple cycles of high-to-low strain. This behavior can also be seen in **Video S1 (SI)**.

To visualize the implications of these rheological measurements, **Figure 2e** shows the impact of increasing the loading of liquid metal particles in the LME as it exits a nozzle. Under three different loading conditions (30, 50 and 80 wt.% EGaIn), we dispensed a single drop from a nozzle. The low loading sample (30 wt.%) spreads across the surface (a glass slide, in this case) as expected from the rheological measurements. In contrast, the high loading (80 wt.%) holds a roughly semi-spherical shape after being dispensed and does not flow outwardly over time due to its viscoelastic behavior.

In summary, the rheological studies show that adding liquid metal particles to an otherwise low-viscosity silicone can increase the viscosity, produce shear-thinning behavior, and ultimately form gel-like behavior at high enough loadings. These properties are useful for printing because it allows the ink to exit the nozzle at high shear, yet preserve its shape at low shear.

## 2.2 Patterning

To establish a direct write process for LME, we loaded the ink into a syringe barrel and extruded it via an applied pressure (Nordson Ultimius V) while moving the nozzle relative to the substrate using an XYZ stage. All the patterns shown here were printed at a constant nozzle velocity of 1.2 mm/s (relative to the stage) and made use of the 90 wt.% LME, which displayed the desirable rheological properties (e.g. yield stress, shear-thinning). The patterns were cured at room temperature, with the exception of the multilayer structure shown in **Figure 3d**, which was cured at 60°C. We do not consider polymer curing to impact pattern generation, as the printing occurs over the course of a few minutes, while the pot-life of PDMS at room temperature is two hours.<sup>61</sup> **Figure 3a** shows examples of LME patterned in a circular and square spiral. **Figure 3b** shows an optical micrograph of an LME spiral with features  $\sim 400$   $\mu\text{m}$  in diameter and a consistent gap of  $\sim 90$   $\mu\text{m}$  between features.

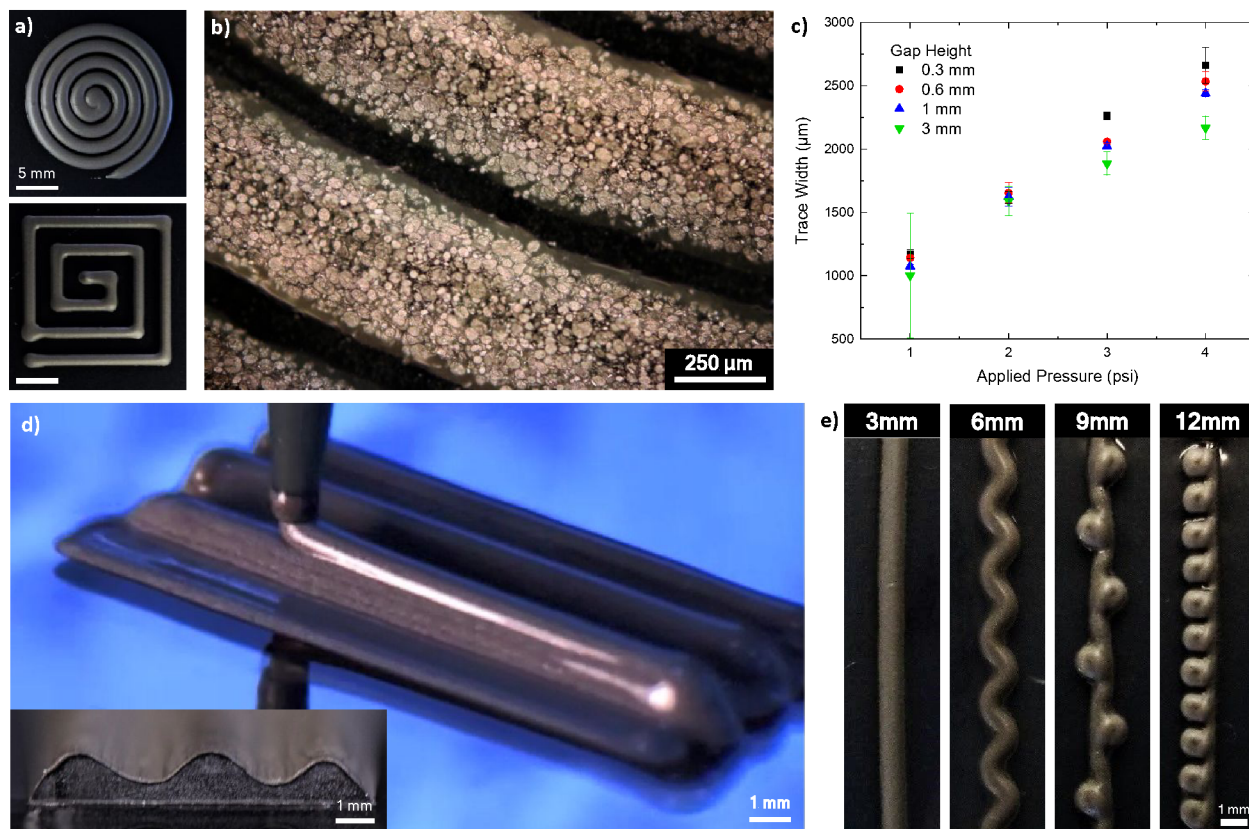


**Figure 3.** Printed LME structures. a) Photographs of LME structures composed of 90 wt.% EGaIn printed from an 18 ga nozzle. b) Optical micrograph of printed LME lines showing 400  $\mu\text{m}$  features with a gap of  $\sim 80$   $\mu\text{m}$  between features, printed from a 25 ga nozzle. c) Plot of trace width as a function of applied pressure for changing gap heights between needle and substrate using a 20 ga nozzle. d) Multi-layer printing forms 3D structures using an 18 ga nozzle. e) Examples of

coiling instabilities that form at large gap heights (the gap heights are listed at the top of the images). Velocity is constant across samples and patterns were printed using an 18 ga nozzle.

The resolution of printed features depends primarily on the applied pressure and the gap height during printing (*i.e.* the distance of the needle from the substrate). Stable traces form by extrusion through a 20 ga nozzle (ID = 0.603 mm) at gap heights between 0.3 mm and 3 mm for pressures between 1 and 3 psi, as summarized in **Figure 3c**. In general, increasing the applied pressure resulted in wider traces, as expected. It is also apparent that when the nozzle is closer to the substrate (smaller gap height), the resulting traces are slightly wider, suggesting the ink gets pushed further laterally. Smaller resolution features are possible to produce by using a nozzle with a smaller diameter. The features are not limited to 2D. **Figure 3d** shows an example of layer-by-layer printing of a 3D structure, and the inset image shows a cross sectional image of the sample after curing. Printing can also be seen in **Video S2 (SI)**.

Moving to gap heights beyond 3 mm, we observed coiling instabilities in the extruded filament, such as those reported in previous literature for other materials.<sup>62–66</sup> The patterns shown in **Figure 3e** were all printed at 2 psi. Printing with a gap height of 3 mm produced a straight line which directly followed the path of the needle. At 6 mm, we observed a “meandering” pathway, where the ink formed a periodic wave pattern despite the needle traveling in a straight line. At 9 mm, the pathway formed complete loops on alternating sides of the path. At 12 mm, the extruded filament formed repeating loops on the same side of the line. The four pictured coiling regimes vary with the height of the nozzle, but prior work has shown that the instability can also be a function of the nozzle velocity.<sup>64</sup> Although it was not our goal to create such features, we include them here because they are interesting and because it highlights behavior made possible by the non-Newtonian rheology. These patterns may be undesirable for direct write printing of targeted geometries by computer-aided design; however, they may be useful for building in additional functionality or geometry-enabled stretchability into the resulting patterns.

### 2.3 Sedimentation to Form Self-Insulating Conductive Pathways

The liquid metal particles are significantly denser than the silicone (the density of liquid metal is 6.25g/mL<sup>67</sup> compared to 1.03 g/mL for PDMS<sup>61</sup>) and therefore can settle over time. Previous work has used this feature to cast films with alternating layers of conductive liquid metal and insulating polymer.<sup>68</sup> Curing the polymer slowly allows time for the particles to settle to the bottom of the structure, resulting in an upper layer rich in silicone and a lower layer rich in liquid metal particles. Fortunately, this settling happens on longer time scales than the printing, but nevertheless can be harnessed in useful ways. In the case of a printable trace of LME, particles that settle can form a region rich with liquid metal at the bottom of the feature and leave behind an insulating shell similar to an insulated electrical wire. This arrangement of material is particularly desirable for making electrical contacts to electrodes or features on the underlying substrate.

**Figure 4a** shows an example of the resulting film structure when particles are given time to settle. The dark grey layer on the surface is depleted in EGaln (enriched in silicone), containing only a low concentration of very small (<2  $\mu\text{m}$ ) particles. The bottom layer is rich in EGaln and therefore appears silver in color.

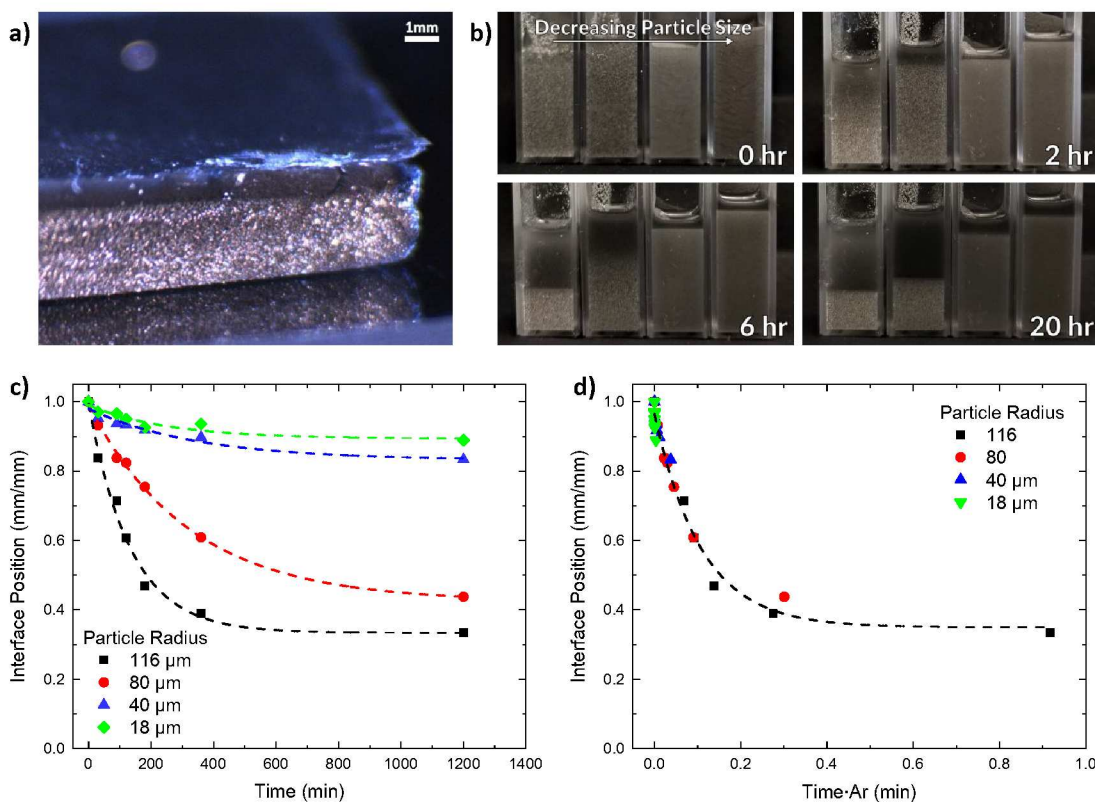


**Figure 4.** Liquid metal particles can settle within uncured silicone. a) Resulting layered structure from curing a composite film slowly, showing an EGaln rich layer on the bottom and an EGaln depleted layer on the top surface. b) Images of the settling behavior of particles of different sizes, shown from large (116  $\mu\text{m}$ ) to small (18  $\mu\text{m}$ ) with respect to time. Larger particles settle more rapidly, as expected. c) Plot of the position of the interface between EGaln rich and EGaln depleted zones. Dashed lines are best-fits of the data. d) Including the Archimedes' number in the x-axis results in the four curves collapsing into one master curve tracking the particle settling behavior.

To evaluate the settling, samples with liquid metal particles of different radii were prepared via mixing on a Vortex mixer for 1 minute or 5 minutes, and by high shear planetary mixing in a Thinky mixer for 1 minute or 3 minutes. The resulting composites had average particle radii of 116 ( $\pm 51$ ), 80 ( $\pm 35$ ), 40 ( $\pm 8$ ), and 18 ( $\pm 5$ )  $\mu\text{m}$ , respectively. The particles were measured via image analysis, as depicted in **Figure S3 (SI)**. The settling behavior of the particles over time is shown visually in **Figure 4b**. It was observed that the samples with larger particles segregated more quickly than the samples with smaller particles. As shown in **Figure 4b**, the sedimentation of particles occurs over the course of hours, while printing of features takes on the order of minutes. Thus, sedimentation is not a major concern during printing, but only for the resulting patterns. Sylgard 184 has a pot of life of 2 hours,<sup>61</sup> so settling is not likely to occur beyond that time frame when cured at room temperature. For the experiments shown, the samples did not include a cross-linking agent so that the viscosity of the polymer component would not change over time. Sedimentation of the patterns can be avoided by curing the silicone rapidly, but we explored what happens if the silicone cures slowly at room temperature.

**Figure 4c** shows the position of the interface between the liquid metal rich and depleted regions over time, normalized by the initial height of the sample. The analysis of particle sedimentation is complex. Literature reports that the interface between the settled particles and the depleted region moves asymptotically toward a final packing value.<sup>69–71</sup> Here, we observe similar behavior in **Figure 4c**. Initially, the material is well dispersed throughout the entire vial, showing a value of 1. As the particles settle, the interface height decays exponentially as particles become more closely packed and eventually plateaus.

The rate of particle settling in a dilute solution can be approximated by assuming the liquid metal particles undergo Stokes' flow settling through the viscous medium. Taking particles as roughly spherical, the particles will fall through the fluid at a rate determined by the balance of gravity and viscous drag, defined by the following equation

$$v_T = \frac{2(\rho_{LM} - \rho_{PDMS})}{9\mu} gr^2 \quad [3]$$

where  $v_T$  is the velocity,  $\rho_{LM}$  is the density of the liquid metal,  $\rho_{PDMS}$  is the density of the silicone matrix,  $\mu$  is the viscosity of the fluid,  $g$  is acceleration due to gravity, and  $r$  is the particle radius. A liquid metal particle in a silicone medium reaches terminal velocity in a matter of seconds (SI). We can estimate the velocity based on the slope of the fit of the data in **Figure 4c**. We find that the particle settling obeys Stokes law at the onset of settling (**Figure S4, SI**), but deviates thereafter, presumably due to the effects of particles on the viscosity. As the particles settle, the local concentration increases, the viscosity increases, and the velocity drops. Thus, we explored other ways of evaluating the data.

Including the effect of particle size in the x-axis causes these lines to collapse into a single plot, shown in **Figure 4d**. This is arrived at by including the Archimedes' number, which is a dimensionless quantity representing the relative impact of gravitational forces to viscous forces. It commonly arises where motion in a fluid is driven by density differences, as is the case here. The Archimedes' number is expressed in Equation 4.

$$Ar = \frac{\rho_{PDMS}(\rho_{LM} - \rho_{PDMS})}{\mu^2} gr^3 \quad [4]$$

When time is multiplied by the Archimedes number of each particle, the data collapses as a single curve (**Figure 4d**). The equations and fitting parameters for the best-fit curves shown in **Figure 4c** and **Figure 4d** are summarized in **Table S2 (SI)**. It is clear from this analysis that formulating an ink with larger particles makes settling faster. Thus, control of particle size and concentration enable selective tuning of LME ink sedimentation and rheological behavior, respectively. For self-insulating structures large particles are desirable to drive particle segregation.

#### 2.4 Inducing Electrical Conductivity

A common problem arising when working with pure liquid metals is the need for an additional encapsulation step following patterning to prevent damage from handling and enable more robust use cases, especially for wearable or on-body applications which take advantage of soft conductors.<sup>72</sup> One approach is to inject liquid metal into silicone microchannels, but this requires fabrication of microchannels.<sup>73–75</sup> Another common approach is drop casting silicones over the liquid metal pattern to encase the patterned structures.<sup>14</sup> The LME composite ink presented in this work does not require any post-processing encapsulation steps. After curing, the liquid metal-elastomer composite preserves its shape and can be stretchable.

The printed patterns are naturally electrically insulating, which may be useful for thermal or dielectric applications. However, for applications that require electrical conductivity, the particles must be sintered. This can be done by mechanically rupturing the thin silicone walls that separate the liquid metal particles can form a conductive, percolated pathway. In literature, liquid metal particles have been ruptured using freezing,<sup>43,76</sup> laser sintering,<sup>77,78</sup> peeling<sup>79</sup> or directed shear force (referred to as mechanical sintering).<sup>41,42,80</sup> Some groups have reported natively conductive composites which are highly concentrated via sedimentation,<sup>44,45,81</sup> although it is possible with particles packed very closely that handling of the samples may provide enough physical input to sinter the particles together. In this work, mechanical force was found to be an effective method to induce conductivity accomplished via two methods: 1) localized pressure and 2) peeling. We show here these two approaches can be applied to the printed LME structures.

Rendering the composites conductive requires a high local concentration of liquid metal particles to form a percolated network. This could be accomplished by simply loading an extremely high concentration (>95 wt.%) of liquid metal into the composite.<sup>82</sup> However, this may result in liquid metal rupturing outside the LME under an applied pressure or smearing when handled, which could short a circuit or leave unwanted residue on other components. To avoid these issues, our approach was to let the particles settle and form a highly concentrated region at the bottom of the LME patterns. By allowing the liquid metal particles to settle and concentrate, the applied pressure will not cause any leakage of liquid metal from the patterns.

A schematic of the sintering process is shown in **Figure 5a**. The applied pressure (indicated by the red arrow) causes particles to merge as motion is carried out across the surface. The sections where particles have merged carry electrical charge through the LME pattern. We applied pressure by use of a hand-held roller. The roller was drawn back and forth across the patterned LME while applying manual pressure to the surface. Under certain conditions,

this action formed a percolated network of LM particles in the composite when we used larger particles ( $\sim 80 \mu\text{m}$ ). Smaller particles are stiffer, which makes them harder to rupture.<sup>40,83–85</sup> Patterns formed with smaller particles either remained insulating or required such extreme pressure to form a percolated pathway that the feature was damaged irreversibly. Additionally, the non-spherical shape of larger particles makes them more likely to contact neighboring particles, which aid in reaching the percolation threshold. Larger particles also have fewer particle-particle junctions.

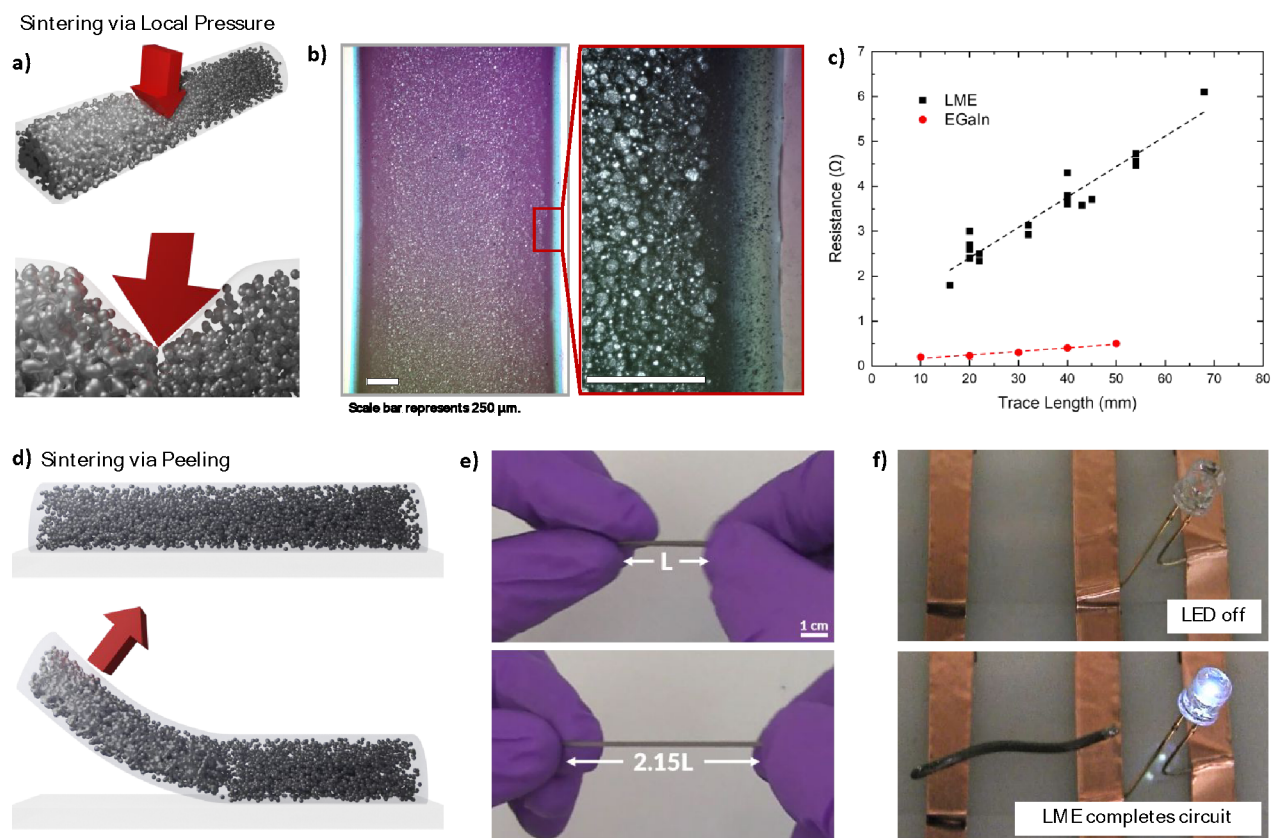


**Figure 5.** a) Schematic representation of the mechanical sintering of particles via applied pressure. After applying pressure, the particles rupture and merge together, forming a percolated and therefore conductive network. d) An optical micrograph taken under polarized light of the underside of a printed line, showing the transition regions from pure polymer shell on the exterior to concentrated liquid metal particles in the interior. Scale bars represent 250 microns. c) Plot comparing the resistance of the conductive composite with bulk liquid metal at varying trace lengths, with linear fits shown as dashed lines. d) Schematic of mechanical sintering via peeling. e) LME trace being stretched after curing and peeling the trace off a glass slide substrate. The LME can be stretched over 2x its initial length. f) Showing an activated LME line being used to complete an LED circuit.

**Figure 5b** is an optical micrograph of the underside of a printed line. In this image it is clear to see the distinct zones formed during printing, an interior region highly concentrated with liquid metal particles and an exterior layer that is depleted of liquid metal, which functions as electrical insulation. We hypothesize that as particles settle, the depleted regions of PDMS may also experience some degree of reflow down the exterior of the printed trace, resulting in this encapsulating edge. **Figure 5c** plots the measured resistance of printed lines as trace length increases and compares the LME composite resistance with that of pure EGaIn traces. The LME patterns show a resistivity of  $\sim 0.7 \Omega/\text{cm}$ , which is approximately an order of magnitude greater than the bulk metal, and slightly higher than reported values for conductive LME composites.<sup>42,43</sup> Projecting the best fit lines from the plot in **Figure 5c** to the y-intercept (a trace length of 0 mm) can be used to gauge the contact resistance of the features. The contact resistance of the pure EGaIn features was  $< 0.1 \Omega$ , while the contact resistance of the LME features was approximately an order of magnitude greater at  $1.0 \Omega$ .

We also found that peeling samples off of the substrate could induce electrical conductivity, as expected from prior studies.<sup>79</sup> Printing traces between two copper pads presented no measurable conductivity, in spite of particles settling to the bottom. However, after peeling the patterns off the substrate they were rendered conductive. Peeling provides local stress on the particles, causing them to rupture and merge. In this case it is achieved by peeling directly from the printing substrate, as illustrated schematically in **Figure 5d**. This can be done either by casting polymer over the

top of the patterns and peeling them uniformly or by peeling individual traces. To demonstrate this principle, we printed LME traces onto a glass slide using the 90 wt.% EGaIn loading. After curing, the patterns were manually peeled off the glass slide, which can be seen in **Video S3 (SI)**. The action of removing the pattern from the slide provides enough mechanical force to sinter the liquid metal particles and form a conductive pattern. **Figure 5e** shows an example of free-standing printed LME structure which has been peeled off of the glass slide substrate, and can be stretched to more than twice its original length. **Figure 5f** shows a similarly prepared LME line being used to complete a circuit and light an LED, which is also shown in **Video S4 (SI)**. When placed with the conductive face downward the LED illuminates, but with the conductive face upward the circuit remains disconnected (due to the settled liquid metal particles, the printed trace has an insulating shell on one side). After peeling, the underside of these features may be prone to leaking due to the highly concentrated liquid metal particles. Thus, it is important to ensure the patterns are attached well to any final substrate. These printed lines form soft conductors that can be used to form stretchable and soft circuits. The biphasic structure is unique for printed conductors and allows us to bypass the usual follow up step of encapsulation.

### 3 Conclusions

This work demonstrates how inclusions of liquid metal within a silicone have a significant impact on the rheological behavior of the composite, thereby enabling them to be utilized for direct write printing. By tuning the ink composition, the viscosity can increase by more than two orders of magnitude, and induce shear-thinning behavior, which makes direct write patterning possible. Such liquid metal elastomer (LME) structures have been shown to have interesting thermal, dielectric, mechanical, and electrical properties. Thus, the ability to print them has implications for a wide range of applications including actuators, soft robotics, thermal interface materials, and stretchable conductors.

By thermally curing the printed structures immediately, the particles remain dispersed in the printed structure. However, by curing the printed structures at room temperature, the particles have time to settle. Larger particles settle through the LME faster than smaller particles. Such settling can produce metal-enriched regions at the bottom surface of the printed feature, surrounded by an insulating silicone shell at the top surface. The bottom surface can be rendered conductive either by direct pressure or by peeling of the sample. Thus, the printed features can function as soft conductors with “self-insulating” shells. This removes the need to encapsulate printed structures, which is often necessary when printing pure liquid metal features.

## 4 Experimental

### 4.1 Materials

The liquid metal used here is a eutectic alloy of gallium and indium (75.5 wt.% Ga, 24.5 wt.% In), purchased from The Indium Corporation. The liquid metal has a melting point of 15.5°C.<sup>86,87</sup> Thus, it is liquid at room temperature. The metal forms a thin native oxide, which provides a mechanical shell around a fluid that otherwise has a very high surface tension ( $\sim 640 \text{ mN}\cdot\text{m}^{-1}$ )<sup>87</sup> and low viscosity ( $\sim 2 \text{ mPa}\cdot\text{s}$ ).<sup>88</sup>

The ink is composed of particles of a eutectic alloy of gallium and indium (75.5wt.% Ga, 24.5wt.% In) distributed in a polydimethylsiloxane (PDMS) matrix (Sylgard 184, Dow). The ink is prepared utilizing a high-shear planetary mixer (Thinky AR-250) or a vortex mixer (VWR) to mix liquid metal into PDMS. The resulting material contains liquid metal particles with diameters between 1 and 175 microns as measured via optical microscopy. Particles were taken to be roughly spherical, although the mixing strategy may also produce some non-spherical particles.

The LME inks used in this work are prepared by shear mixing EGaIn with PDMS (Sylgard 184, Dow Corning). The PDMS was prepared in a 10:1 base to curing agent weight ratio. The materials were mixed in varying ratios of liquid metal to PDMS. The samples prepared in this work were 0, 30, 50, 70, 80, and 90 wt.% liquid metal, with the remainder being PDMS. After mixing, the resulting ‘ink’ consisted of a dispersion of liquid metal particles within an uncured elastomer matrix.

By varying the mixing time and conditions, particles of different sizes could be formed. A planetary mixer (Thinky AR-250) was used for high-shear mixing, generating small particles, and an Analog Vortex Mixer (VWR) was used for producing larger particles. Particle size was measured through image analysis of optical micrographs using ImageJ.

## 4.2 Rheological Characterization

Rheology experiments were conducted using an AR-G2 rheometer from TA Instruments, equipped with a 40 mm parallel plate geometry. Materials were pre-sheared to minimize any impact that sample handling may have on the resulting measurements. The specific steps are discussed in further detail in the Supporting Information.

## 4.3 Electrical Characterization

A handheld multimeter was used to confirm traces were electrically conductive. Resistance measurements were obtained using a Keithley 2400 Sourcemeter (Keithley Instruments).

## 4.4 Printing

The materials were printed using a printer developed in our lab, utilizing a 3-axis stage (Minitech Machinery Corporation) and a pressure actuator (Nordson EFD Ultimius V). Inks were loaded into syringe barrels with Luer lock connecting nozzles, allowing for quick changes to extrusion nozzle diameters. The syringe barrels were loaded into custom 3D printed parts to secure the barrel to the stage. Motion was controlled via the Mach3 software CNC program (Newfangled Solutions Software). The printer is shown in **Figure S5 (SI)**.

## Conflicts of interest

There are no conflicts to declare.

## Acknowledgements

The authors acknowledge Minyung Song for useful discussion and her input on experimental design. The authors also acknowledge Luke Cunningham for his assistance in producing graphics, specifically in Figure 5. This work was supported by the Center for Advanced Self-Powered Systems of Integrated Sensors and Technologies (ASSIST).

## References

- 1 M. Amjadi, A. Pichitpajongkit, S. Lee, S. Ryu and I. Park, *ACS Nano*, 2014, **8**, 5154–5163.
- 2 J. T. Muth, D. M. Vogt, R. L. Truby, Y. Mengüç, D. B. Kolesky, R. J. Wood and J. A. Lewis, *Adv. Mater.*, 2014, **26**, 6307–6312.
- 3 Z. Li, T. Le, Z. Wu, Y. Yao, L. Li, M. Tentzeris, K.-S. Moon and C. P. Wong, *Adv. Funct. Mater.*, 2015, **25**, 464–470.
- 4 J. E. Q. Quinsaat, I. Burda, R. Krämer, D. Häfliger, F. A. Nüesch, M. Dascalu and D. M. Opris, *Scientific Reports*, 2019, **9**, 1–11.
- 5 A. Saleem, L. Frommann and A. Soever, *Polymers*, 2010, **2**, 200–210.
- 6 H. Hong, Y. H. Jung, J. S. Lee, C. Jeong, J. U. Kim, S. Lee, H. Ryu, H. Kim, Z. Ma and T. Kim, *Advanced Functional Materials*, 2019, **29**, 1902575.
- 7 G. Gallone, F. Carpi, D. De Rossi, G. Levita and A. Marchetti, *Materials Science and Engineering: C*, 2007, **27**, 110–116.
- 8 J. E. Q. Quinsaat, M. Alexandru, F. A. Nüesch, H. Hofmann, A. Borgschulte and D. M. Opris, *J. Mater. Chem. A*, 2015, **3**, 14675–14685.
- 9 C. Dodd, *Proceedings of the Physical Society. Section B*, 1950, **63**, 662–664.
- 10 T. Dd, *Clin Chem*, 1977, **23**, 719–724.
- 11 A. Burdakin, B. Khlevnoy, M. Samoylov, V. Sapritsky, S. Ogarev, A. Panfilov, G. Bingham, V. Privalsky, J. Tansock and T. Humpherys, *Metrologia*, 2008, **45**, 75.
- 12 A. R. Jacob, D. P. Parekh, M. D. Dickey and L. C. Hsiao, *Langmuir*, 2019, **35**, 11774–11783.
- 13 M. D. Dickey, *Advanced Materials*, 2017, **29**, 1606425.
- 14 D. P. Parekh, C. Ladd, L. Panich, K. Moussa and M. D. Dickey, *Lab Chip*, 2016, **16**, 1812–1820.
- 15 A. Cook, D. P. Parekh, C. Ladd, G. Kotwal, L. Panich, M. Durstock, M. D. Dickey and C. E. Tabor, *Advanced Engineering Materials*, 2019, **21**, 1900400.
- 16 C. Ladd, J.-H. So, J. Muth and M. D. Dickey, *Adv. Mater.*, 2013, **25**, 5081–5085.

- 17 Y.-G. Park, H. S. An, J.-Y. Kim and J.-U. Park, *Science Advances*, 2019, **5**, eaaw2844.
- 18 Y. Yoon, S. Kim, D. Kim, S. K. Kauh and J. Lee, *Advanced Materials Technologies*, 2019, **4**, 1800379.
- 19 U. Daalkhajav, O. D. Yirmibesoglu, S. Walker and Y. Mengüç, *Advanced Materials Technologies*, 2018, **3**, 1700351.
- 20 W. Kong, Z. Wang, M. Wang, K. C. Manning, A. Uppal, M. D. Green, R. Y. Wang and K. Rykaczewski, *Advanced Materials*, 2019, **31**, 1904309.
- 21 H. Chang, pan zhang, R. Guo, Y. Cui, Y. Hou, Z. Sun and W. Rao, *ACS Appl. Mater. Interfaces*, , DOI:10.1021/acsami.9b20430.
- 22 R. K. Kramer, C. Majidi and R. J. Wood, *Adv. Funct. Mater.*, 2013, **23**, 5292–5296.
- 23 J. W. Boley, E. L. White, G. T.-C. Chiu and R. K. Kramer, *Advanced Functional Materials*, 2014, **24**, 3501–3507.
- 24 M. G. Mohammed and R. Kramer, *Advanced Materials*, 2017, **29**, 1604965.
- 25 Y. He, L. Zhou, J. Zhan, Q. Gao, J. Fu, C. Xie, H. Zhao and Y. Liu, *3D Printing and Additive Manufacturing*, 2018, **5**, 195–203.
- 26 L.-Y. Zhou, Q. Gao, J.-F. Zhan, C.-Q. Xie, J.-Z. Fu and Y. He, *ACS Appl. Mater. Interfaces*, 2018, **10**, 23208–23217.
- 27 H. Yan, Y. Chen, Y. Deng, L. Zhang, X. Hong, W. Lau, J. Mei, D. Hui, H. Yan and Y. Liu, *Appl. Phys. Lett.*, 2016, **109**, 083502.
- 28 S. H. Jeong, S. Chen, J. Huo, E. K. Gamstedt, J. Liu, S.-L. Zhang, Z.-B. Zhang, K. Hjort and Z. Wu, *Scientific Reports*, 2015, **5**, 1–10.
- 29 N. Kazem, T. Hellebrekers and C. Majidi, *Advanced Materials*, 2017, **29**, 1605985.
- 30 A. Fassler and C. Majidi, *Adv. Mater.*, 2015, **27**, 1928–1932.
- 31 M. D. Bartlett, A. Fassler, N. Kazem, E. J. Markvicka, P. Mandal and C. Majidi, *Advanced Materials*, 2016, **28**, 3726–3731.
- 32 N. Kazem, M. D. Bartlett and C. Majidi, *Advanced Materials*, 2018, **30**, 1706594.
- 33 Y. Sargolzaeiaval, V. P. Ramesh, T. V. Neumann, R. Miles, M. D. Dickey and M. C. Öztürk, *ECS J. Solid State Sci. Technol.*, 2019, **8**, P357–P362.
- 34 M. G. Saborio, S. Cai, J. Tang, M. B. Ghasemian, M. Mayyas, J. Han, M. J. Christoe, S. Peng, P. Koshy, D. Esrafilzadeh, R. Jalili, C. H. Wang and K. Kalantar-Zadeh, *Small*, 2020, **16**, 1903753.
- 35 G. Yun, S.-Y. Tang, S. Sun, D. Yuan, Q. Zhao, L. Deng, S. Yan, H. Du, M. D. Dickey and W. Li, *Nature Communications*, 2019, **10**, 1–9.
- 36 M. D. Bartlett, N. Kazem, M. J. Powell-Palm, X. Huang, W. Sun, J. A. Malen and C. Majidi, *PNAS*, 2017, **114**, 2143–2148.
- 37 R. Tutika, S. H. Zhou, R. E. Napolitano and M. D. Bartlett, *Advanced Functional Materials*, 2018, **28**, 1804336.
- 38 L. Zhao, H. Liu, X. Chen, S. Chu, H. Liu, Z. Lin, Q. Li, G. Chu and H. Zhang, *J. Mater. Chem. C*, 2018, **6**, 10611–10617.
- 39 C. Pan, E. J. Markvicka, M. H. Malakooti, J. Yan, L. Hu, K. Matyjaszewski and C. Majidi, *Advanced Materials*, 2019, **31**, 1900663.
- 40 J. W. Boley, E. L. White and R. K. Kramer, *Advanced Materials*, 2015, **27**, 2355–2360.
- 41 Y. Lin, C. Cooper, M. Wang, J. J. Adams, J. Genzer and M. D. Dickey, *Small*, 2015, **11**, 6397–6403.
- 42 E. J. Markvicka, M. D. Bartlett, X. Huang and C. Majidi, *Nature Materials*, 2018, **17**, 618.
- 43 L. Zhou, J. Fu, Q. Gao, P. Zhao and Y. He, *Advanced Functional Materials*, 2020, **30**, 1906683.
- 44 Y. Wang, Z. Yu, G. Mao, Y. Liu, G. Liu, J. Shang, S. Qu, Q. Chen and R.-W. Li, *Advanced Materials Technologies*, 2019, **4**, 1800435.
- 45 Z. Yu, J. Shang, X. Niu, Y. Liu, G. Liu, P. Dhanapal, Y. Zheng, H. Yang, Y. Wu, Y. Zhou, Y. Wang, D. Tang and R.-W. Li, *Advanced Electronic Materials*, 2018, **4**, 1800137.
- 46 J. W. Boley, W. M. van Rees, C. Lissandrello, M. N. Horenstein, R. L. Truby, A. Kotikian, J. A. Lewis and L. Mahadevan, *PNAS*, 2019, **116**, 20856–20862.
- 47 V. Ozbolat, M. Dey, B. Ayan, A. Povilianskas, M. C. Demirel and I. T. Ozbolat, *ACS Biomater. Sci. Eng.*, 2018, **4**, 682–693.
- 48 S. Roh, D. P. Parekh, B. Bharti, S. D. Stoyanov and O. D. Velev, *Advanced Materials*, 2017, **29**, 1701554.
- 49 A. Hamidi and Y. Tadesse, *Materials & Design*, 2020, **187**, 108324.
- 50 Z. Qin, B. G. Compton, J. A. Lewis and M. J. Buehler, *Nat Commun*, , DOI:10.1038/ncomms8038.

- 51 J. R. Tumbleston, D. Shirvanyants, N. Ermoshkin, R. Januszewicz, A. R. Johnson, D. Kelly, K. Chen, R. Pinschmidt, J. P. Rolland, A. Ermoshkin, E. T. Samulski and J. M. DeSimone, *Science*, 2015, aaa2397.
- 52 T. G. Mason, *Current Opinion in Colloid & Interface Science*, 1999, **4**, 231–238.
- 53 J. Mewis and N. J. Wagner, *Colloidal Suspension Rheology*, Cambridge University Press, 2011.
- 54 C. Ancey and H. Jorrot, *Journal of Rheology*, 2001, **45**, 297–319.
- 55 R. Tutika, S. Kmiec, A. B. M. T. Haque, S. W. Martin and M. D. Bartlett, *ACS Appl. Mater. Interfaces*, 2019, **11**, 17873–17883.
- 56 C. W. Macosko, *Rheology: Principles, Measurements, and Applications*, Wiley-VCH, 1st edn., 1994.
- 57 H. H. Winter and F. Chambon, *Journal of Rheology*, 1986, **30**, 367–382.
- 58 H. H. Winter, John Wiley & Sons, New York, 1989.
- 59 N. A. Burns, M. A. Naclerio, S. A. Khan, A. Shojaei and S. R. Raghavan, *Journal of Rheology*, 2014, **58**, 1599–1614.
- 60 S. R. Raghavan and S. A. Khan, *Journal of Rheology*, 1995, **39**, 1311–1325.
- 61 SYLGARD® 184 SILICONE ELASTOMER KIT, <http://www.dowcorning.com/applications/search/products/Details.aspx?prod=01064291>, (accessed February 27, 2017).
- 62 R. Passieux, L. Guthrie, S. H. Rad, M. Lévesque, D. Therriault and F. P. Gosselin, *Advanced Materials*, 2015, **27**, 3676–3680.
- 63 P.-T. Brun, C. Inamura, D. Lizardo, G. Franchin, M. Stern, P. Houk and N. Oxman, *Philos Trans A Math Phys Eng Sci*, DOI:10.1098/rsta.2016.0156.
- 64 N. M. Ribe, M. Habibi and D. Bonn, *Annu. Rev. Fluid Mech.*, 2011, **44**, 249–266.
- 65 X. Tian, J. Plott, H. Wang, B. Zhu and A. J. Shih, *Procedia CIRP*, 2017, **65**, 196–201.
- 66 H. Yuk and X. Zhao, *Advanced Materials*, 2018, **30**, 1704028.
- 67 M. J. Assael, I. J. Armyra, J. Brillo, S. V. Stankus, J. Wu and W. A. Wakeham, *Journal of Physical and Chemical Reference Data*, 2012, **41**, 033101.
- 68 L. Zhu, Y. Chen, W. Shang, S. Handschuh-Wang, X. Zhou, T. Gan, Q. Wu, Y. Liu and X. Zhou, *J. Mater. Chem. C*, 2019, **7**, 10166–10172.
- 69 F. Concha and M. C. Bustos, *AIChE Journal*, 1987, **33**, 312–315.
- 70 G. J. Kynch, *Trans. Faraday Soc.*, 1952, **48**, 166–176.
- 71 E. Torfs, S. Balemans, F. Locatelli, S. Diehl, R. Bürger, J. Laurent, P. François and I. Nopens, *Water Research*, 2017, **110**, 38–47.
- 72 Y. Sargolzaeiaval, V. Padmanabhan Ramesh, T. V. Neumann, V. Misra, D. Vashae, M. D. Dickey and M. C. Öztürk, *Applied Energy*, 2020, **262**, 114370.
- 73 M. D. Dickey, R. C. Chiechi, R. J. Larsen, E. A. Weiss, D. A. Weitz and G. M. Whitesides, *Adv. Funct. Mater.*, 2008, **18**, 1097–1104.
- 74 Y. Lin, O. Gordon, M. R. Khan, N. Vasquez, J. Genzer and M. D. Dickey, *Lab on a Chip*, 2017, **17**, 3043–3050.
- 75 S.-Y. Tang, Y. Lin, I. Joshipura, K. Khoshmanesh and M. Dickey, *Lab Chip*, DOI:10.1039/C5LC00742A.
- 76 H. Wang, Y. Yao, Z. He, W. Rao, L. Hu, S. Chen, J. Lin, J. Gao, P. Zhang, X. Sun, X. Wang, Y. Cui, Q. Wang, S. Dong, G. Chen and J. Liu, *Advanced Materials*, 2019, **31**, 1901337.
- 77 S. Liu, M. C. Yuen, E. L. White, J. W. Boley, B. Deng, G. J. Cheng and R. Kramer-Bottiglio, *ACS Appl. Mater. Interfaces*, 2018, **10**, 28232–28241.
- 78 S. Liu, S. N. Reed, M. J. Higgins, M. S. Titus and R. Kramer-Bottiglio, *Nanoscale*, 2019, **11**, 17615–17629.
- 79 L. Tang, S. Cheng, L. Zhang, H. Mi, L. Mou, S. Yang, Z. Huang, X. Shi and X. Jiang, *iScience*, 2018, **4**, 302–311.
- 80 B. Chen, M. Kruse, B. Xu, R. Tutika, W. Zheng, M. D. Bartlett, Y. Wu and J. C. Claussen, *Nanoscale*, 2019, **11**, 5222–5230.
- 81 X. Yi, Z. Yu, X. Niu, J. Shang, G. Mao, T. Yin, H. Yang, W. Xue, P. Dhanapal, S. Qu, G. Liu and R.-W. Li, *Advanced Electronic Materials*, 2019, **5**, 1800655.
- 82 A. Koh, J. Sietins, G. Slipper and R. Mrozek, *Journal of Materials Research*, 2018, 1–11.
- 83 N. J. Morris, Z. J. Farrell and C. E. Tabor, *Nanoscale*, 2019, **11**, 17308–17318.
- 84 T. R. Lear, S.-H. Hyun, J. W. Boley, E. L. White, D. H. Thompson and R. K. Kramer, *Extreme Mechanics Letters*, 2017, **13**, 126–134.

## ARTICLE

## Journal Name

85 Z. J. Farrell and C. Tabor, *Langmuir*, 2018, **34**, 234–240.

86 J. E. Inglesfield, *J. Phys. C: Solid State Phys.*, 1968, **1**, 1337–1346.

87 D. Zrnic and D. S. Swatik, *Journal of the Less Common Metals*, 1969, **18**, 67–68.

88 J. N. Koster, *Crystal Research and Technology*, 1999, **34**, 1129–1140.